Triaxiality and state-dependent shape properties of Xe isotopes

A. I. Budaca[1] and R. Budaca[1,2]
[1] *"Horia Hulubei" National Institute for Physics and Nuclear Engineering, Str. Reactorului 30, RO-077125, POB-MG6 Bucharest-Măgurele, Romania*
[2] *Academy of Romanian Scientists, 54 Splaiul Independenţei, RO-050094, Bucharest, Romania*

(Received 19 February 2020; accepted 2 June 2020; published 18 June 2020)

The low-lying collective spectra for an extended set of Xe nuclei are described within a phenomenological Bohr model with an exactly separable collective potential. The dependence of the collective potential on the γ shape variable is chosen to allow the description of a phase transition between axial and triaxial shapes, while the β excitations are described within the formalism of energy-dependent potentials in order to accommodate the different structure of the excited states. The combined contribution of these effects leads to a high fidelity description of the experimental spectra for $^{118-128}$Xe isotopes, especially in the excited rotational bands, which revealed a rapid onset of stable triaxial deformation in the ^{120}Xe nucleus persisting also in the heavier isotopes. The critical nature of ^{120}Xe is also reflected in its very strong state-dependence of the deformation properties.

DOI: 10.1103/PhysRevC.101.064318

I. INTRODUCTION

The Xe nuclei mark the low mass boundary of a region in the nuclide chart where the triaxial deformation manifests itself in various ways, be it through specific γ band patterns [1,2], or emergence of wobbling [3–7] and chiral bands [8] associated usually to rigid triaxial shapes. The diversity of energy spectra encountered in the Xe isotopic chain provides a good opportunity to study various shape phase transitions as a function of neutron number variation and the validity of dynamical symmetries [9,10]. The more recent theoretical efforts in this direction are based on phenomenological [11–17] and microscopically derived [18–21] Bohr Hamiltonian (BH) [22,23] approaches, interacting boson model (IBM) [24–28], and fully microscopical formalisms [28–32]. Most of these studies are usually focused on few Xe nuclei in the $A \approx 130$ mass region, whose collective behavior is commonly concluded to be $O(6)$-like (γ unstable) with hints of stable triaxial deformation [33]. This draws attention to Xe nuclei from the perspective of the neverending quest for triaxial shapes in nuclear systems. The knowledge of the deformation related collective properties of Xe isotopes is also important for the study of the double β decay or double electron capture phenomena [34], experimentally observed for ^{136}Xe [35] and, respectively, ^{124}Xe [36] and theoretically predicted to occur in their corresponding neighboring isotopes ^{134}Xe and ^{126}Xe [37].

The phenomenological approaches to five-dimensional collective dynamics are presently sufficiently well developed to describe essentially any type of collective spectra with very high accuracy. Although, it lacks in what concerns the extrapolation to neighboring nuclei, its success in the reproduction of experimental data offers direct and reliable information on the collective dynamics and the actual shape of the considered nuclei. This information must be sought by more sophisticated microscopically driven models as a final result.

In this paper, we propose a separable version of the BH which combines the advantages of the most successful approaches used in connection to the phenomenological geometric model. On one hand, a sufficiently general coupling between the triaxiality and rotational degrees of freedom is treated in a diagonalization procedure specific to the algebraic collective model (ACM) [38–40] which represents a tractable algebraic approach to the solution of the BH essentially for any type of collective potential. On the other hand, the deformation dependence of the nuclear dynamics is simulated within the analytical theory of energy-dependent potentials [41–44]. The detailed theoretical formalism will be exposed in the next section and then applied for the description of the collective spectra of the $^{118-128}$Xe nuclei. The versatile nature of the model, and in consequence its high fidelity reproduction of experimental data will be used as a source of information on nuclear deformation and its state dependence in the considered Xe isotopes.

II. THEORETICAL FORMALISM

The starting point is the general BH with a shape-independent mass [22,23]:

$$H = -\frac{\hbar^2}{2B}\left[\frac{1}{\beta^4}\frac{\partial}{\partial\beta}\beta^4\frac{\partial}{\partial\beta} - \frac{\hat{\Lambda}^2}{\beta^2}\right] + U(\beta,\gamma), \tag{1}$$

where

$$\hat{\Lambda}^2 = -\frac{1}{\sin 3\gamma}\frac{\partial}{\partial\gamma}\sin 3\gamma\frac{\partial}{\partial\gamma} + \sum_{m=1}^{3}\frac{\hat{L}_m^2}{4\sin^2(\gamma - 2\pi m/3)} \tag{2}$$

is the SO(5) Casimir operator, whose action on the angular degrees of freedom is represented by operators of the intrinsic SO(3) angular momentum operators $\hat{L}_m$. For analytical purposes, it is useful to work with reduced energy

and potential:

$$\epsilon = \frac{2B}{\hbar^2}E, \quad u(\beta,\gamma) = \frac{2B}{\hbar^2}U(\beta,\gamma). \tag{3}$$

By considering a reduced potential [45,46]

$$u(\beta,\gamma) = v(\beta) + \frac{w(\gamma)}{\beta^2}, \tag{4}$$

an exact separation of the β variable from the γ-angular ones is possible for Eq. (1) with a factorized total wave function $\Psi(\beta,\gamma,\Omega) = R(\beta)\Phi(\gamma,\Omega)$:

$$\left[-\frac{1}{\beta^4}\frac{\partial}{\partial\beta}\beta^4\frac{\partial}{\partial\beta} + \frac{W}{\beta^2} + v(\beta)\right]R(\beta) = \epsilon R(\beta), \tag{5}$$

$$\left[-\frac{1}{\sin 3\gamma}\frac{\partial}{\partial\gamma}\sin 3\gamma\frac{\partial}{\partial\gamma} + \frac{1}{4}\sum_{m=1}^{3}\frac{\hat{L}_m^2}{\sin^2\left(\gamma - \frac{2}{3}\pi m\right)} + w(\gamma) - W\right]\Phi(\gamma,\Omega) = 0. \tag{6}$$

The potential term $w(\gamma)/\beta^2$ was for the first time discussed in the paper of Wilets and Jean [45], where they state: "*Physically, we expect this to be unrealistic, since γ stability should increase rather than decrease with β*". This is still a valid point, and the potential form (4) is essentially for the separation of the β variable. The separated form of the potential is needed to accommodate the use of energy-dependence for the β potential. Otherwise, for mixed dependence of the potential on β and γ variables, the use of the formalism for energy-dependent potential becomes problematic. First of all, the energy dependence changes the definition of the linear momentum vector by an additional term [57], which will have a vanishing contribution to the associated multidimensional angular momentum only if the potential is isotropic. Another difficulty comes from the fact that for nonseparable multidimensional energy-dependent potentials, the associated equations are not analytically solvable and the extension of the usual approximate methods of quantum mechanics is not necessarily valid because an energy-dependent problem constitutes a coherent quantum theory only in the case of a isotropic potential with a linear energy dependence [57]. Such problems have seldom been studied so that even the existence of solutions is not evident, not to mention their physically correct behavior or uniqueness.

Even if the separable form of the total reduced potential (4) has a more analytical purpose, it was found to be suitable for well-deformed nuclei [47], which are usually characterized by high β excited bands. This disparity between γ-rotational excitations and β excitations is naturally simulated by the centrifugal term W/β^2 for large deformation. Alternatively, the $w(\gamma)$ potential can be understood as a way to generalize the usual SO(5) coupling between γ variable and rotational angles Ω when the total potential is γ-independent.

One considers the γ potential $w(\gamma)$ to be of the form [38]

$$w(\gamma) = c_1(1 - \cos 3\gamma) - c_2(1 - \cos^2 3\gamma), \tag{7}$$

where c_1 and c_2 are adjustable parameters. This potential was introduced by Iachello [48] for the purpose of studying the shape phase transition in the triaxiality variable, because its range of shapes include both axial and triaxial minima with varying softness (shallowness and depth) [38]. Its spectral properties were investigated in Refs. [49,50], where the basic signatures of triaxiality emergence were pointed out. Despite its many useful properties, this potential did not receive much attention in what concerns numerical applications on actual nuclei.

In order to find the solution of the γ-angular equation, the corresponding wave function is expanded in SO(5) spherical harmonics $|\tau\alpha LM\rangle = \mathcal{Y}_{\tau\alpha LM}(\gamma,\Omega)$ [51] indexed by the seniority τ [52], α order distinguishing multiple occurrences of the same angular momentum within a multiplet of fixed seniority, and by angular momentum and its projection on the third intrinsic axis:

$$\Phi^{\kappa}_{LM}(\gamma,\Omega) = \sum_{\tau,\alpha} G^{\kappa}_{\tau\alpha L}\mathcal{Y}_{\tau\alpha LM}(\gamma,\Omega). \tag{8}$$

$G^{\kappa}_{\tau\alpha L}$ are basis expansion amplitudes, with κ being the completeness number distinguishing diagonalization solutions. The kinetic operator $\hat{\Lambda}^2$ is diagonal in the chosen basis [53]:

$$\hat{\Lambda}^2|\tau\alpha LM\rangle = \tau(\tau+3)|\tau\alpha LM\rangle. \tag{9}$$

While the relevant potential terms have the following matrix elements:

$$\langle\tau'\alpha' LM|\cos^n 3\gamma|\tau\alpha LM\rangle = (\tau\alpha L, (3n)10||\tau'\alpha' L)\langle\tau'|||\cos^n 3\gamma|||\tau\rangle, \tag{10}$$

where the first factor is a SO(5) Clebsch-Gordan coefficient [51], whose values can be taken from [40]. The corresponding SO(5)-reduced matrix elements have the following closed expressions for $n = 1$ [38,39]:

$$\langle\tau+1|||\cos 3\gamma|||\tau\rangle = \sqrt{\frac{45\tau(\tau+1)(\tau+4)}{2(2\tau+1)(2\tau+5)(2\tau+7)}}, \tag{11}$$

$$\langle\tau+3|||\cos 3\gamma|||\tau\rangle = \sqrt{\frac{35\tau(\tau+1)(\tau+2)(\tau+3)}{2(2\tau+5)(2\tau+7)(2\tau+9)}}. \tag{12}$$

The $n = 2$ reduced matrix elements are determined by bearing in mind that

$$\mathcal{Y}_{(3n)100}(\gamma,\Omega) = \frac{1}{4\pi}\sqrt{3(2n+1)}P_n(\cos 3\gamma) \tag{13}$$

with $P_n(x)$ denoting a Legendre polynomial [54], and using the empirical formula [38,39]

$$\langle\tau'|||\hat{\mathcal{Y}}_s|||\tau\rangle = \frac{1}{4\pi}\frac{\left(\frac{\sigma}{2}+1\right)!}{\left(\frac{\sigma}{2}-\tau\right)!\left(\frac{\sigma}{2}-s\right)!\left(\frac{\sigma}{2}-\tau'\right)!}\sqrt{\frac{(2\tau+3)(2s+3)}{(\tau'+2)(\tau'+1)}} \times\sqrt{\frac{(\sigma+4)(\sigma-2\tau+1)!(\sigma-2s+1)!(\sigma-2\tau'+1)!}{(\sigma+3)!}}, \tag{14}$$

where $\sigma = \tau + \tau' + s$ and $\hat{\mathcal{Y}}_s$ is a tensorial representation of the SO(5) spherical harmonic. Finally, the eigenvalue for the γ-angular equation will be indexed just by angular momentum L and the completeness number κ. For the convergence of

the diagonalization results, a basis extended up to $\tau = 30$ is enough.

The β potential is chosen to be of the Kratzer type [55,56] and with a coupling constant of the hyperbolic term depending linearly on the energy of the system:

$$v(\beta) = \frac{a_1}{\beta^2} - \frac{1 + a_2\epsilon}{\beta}. \tag{15}$$

Compared to the Davidson potential, which is extensively used for nuclear collective excitations, the Kratzer potential has a smaller slope of the outer wall. This makes the associated wave function to decay more slowly for large β values. Such a behavior affects mostly the β excited states which have a consistent deformation probability distribution near the potential walls. This is an important feature, because the energy spacings between β band states are usually overestimated when using an oscillator-like β potential well. Additionally, the analytical form of the Kratzer potential allows for very deep and narrow wells which can describe transitional nuclei in the same manner as the critical point solutions with an infinite square-well β potential [10]. The use of an energy-dependent potential is justified phenomenologically by the distinct microscopic structure of the excited states, while from the analytical point of view, such a formalism [57] was shown to simulate the Bohr model with a deformation dependent mass [58–60] having however an additional nonlocality, that is a differential term [44].

The associated β differential equation is solved by following up to a certain point the procedure for a state-independent Coulomb potential. There are few alternative approaches for this, which are equivalent in what concerns the final result. Here, we transform Eq. (5) into a Whittaker differential equation [61],

$$f''(x) + \left[\frac{k}{x} - \frac{1}{4} + \frac{\left(\frac{1}{4} - \mu^2\right)}{x^2}\right] f(x) = 0, \tag{16}$$

by making the change of function $f(\beta) = \beta^2 R(\beta)$ and the change of variable $x = 2\sqrt{\varepsilon}\beta$ with the following notations:

$$\varepsilon = -\epsilon, \quad k = \frac{1 - a_2\varepsilon}{2\sqrt{\varepsilon}}, \quad \mu = \sqrt{\frac{9}{4} + W_{L\kappa} + a_1}. \tag{17}$$

A solution of this equation, which is regular in both origin and the asymptotic limit, can be expressed in terms of an associated Laguerre polynomial [54] if the following condition is fulfilled:

$$\mu + \tfrac{1}{2} - k = -n, \tag{18}$$

where n is a positive integer. This condition leads to a quadratic equation for ϵ

$$(1 + a_2\epsilon)^2 + 4\epsilon\left(n + \frac{1}{2} + \sqrt{\frac{9}{4} + W_{L\kappa} + a_1}\right)^2 = 0. \tag{19}$$

Its physical solution is

$$\epsilon_{nL\kappa} = \frac{1}{a_2^2}\left[2\left(n + \frac{1}{2} + \sqrt{\frac{9}{4} + W_{L\kappa} + a_1}\right)\right.$$
$$\times \sqrt{\left(n + \frac{1}{2} + \sqrt{\frac{9}{4} + W_{L\kappa} + a_1}\right)^2 + a_2}$$
$$\left. - 2\left(n + \frac{1}{2} + \sqrt{\frac{9}{4} + W_{L\kappa} + a_1}\right)^2 - a_2\right]. \tag{20}$$

Making the following notations:

$$\eta_{nL\kappa} = \sqrt{-\epsilon} = \frac{1 + a_2\epsilon_{nL\kappa}}{2\left(n + \frac{1}{2} + \sqrt{\frac{9}{4} + W_{L\kappa} + a_1}\right)}, \tag{21}$$

$$p_{L\kappa} = \sqrt{\frac{9}{4} + W_{L\kappa} + a_1} - \frac{3}{2}, \tag{22}$$

the β wave function can then be written in the following analytical closed form [42]:

$$R_{nL\kappa}(\beta) = N_{nL\kappa}\beta^{p_{L\kappa}} e^{-\eta_{nL\kappa}\beta} L_n^{2p_{L\kappa}+3}(2\eta_{nL\kappa}\beta). \tag{23}$$

The normalization constant is determined from the condition

$$\int_0^\infty [R_{nL\kappa}(\beta)]^2 \beta^4 \left(1 + \frac{a_2}{\beta}\right) d\beta = 1, \tag{24}$$

where the modified normalization metric

$$d\beta \rightarrow \left(1 - \frac{\partial v(\beta)}{\partial \epsilon}\right) d\beta, \tag{25}$$

accounts for the energy dependence of the β potential [57] and assures the conservation of the norm. Speculating the properties of the associated Laguerre polynomials [54], the normalization constant acquires the simple expression

$$N_{nL\kappa} = \sqrt{\frac{\eta_{nL\kappa} n!}{\Gamma(n + 2p_{L\kappa} + 4)(a_2\eta_{nL\kappa} + n + p_{L\kappa} + 2)}}$$
$$\times (2\eta_{nL\kappa})^{p_{L\kappa}+2}. \tag{26}$$

Now one can see that the integer number n plays the role of the β excitation quantum number.

III. $E2$ TRANSITIONS

The obtained total wave function $\Psi_{nLM\kappa}(\beta, \gamma, \Omega) = R_{nL\kappa}(\beta)\Phi^{\kappa}_{LM}(\gamma, \Omega)$ is now ready to be employed for the calculation of electromagnetic transition probabilities. The most important data in this sense are related to the quadrupole transitions, which in the present model are calculated with the transition operator

$$T^{(E2)}_{\mu} = \frac{3R^2 Ze}{4\pi}\beta_M \beta \mathcal{Q}_{\mu}, \tag{27}$$

where

$$\mathcal{Q}_{\mu} = D^2_{\mu 0}(\Omega)\cos\gamma + \frac{1}{\sqrt{2}}\left[D^2_{\mu 2}(\Omega) + D^2_{\mu -2}(\Omega)\right]\sin\gamma, \tag{28}$$

while β_M is a scaling factor for the BH variable β which makes the connection to the quadrupole deformation $\beta_2 = \beta_M\beta$, R is the nuclear radius, Z is the charge number. The final quadrupole transition rates are calculated as

$$B(E2; i \rightarrow f) = \left|\left\langle \Psi_{n_i L_i \kappa_i} \middle|\middle| T^{E2}_2 \middle|\middle| \Psi_{n_f L_f \kappa_f} \right\rangle\right|^2 \tag{29}$$

TABLE I. Experimental and theoretical values of the commonly used spectral and electromagnetic transition observables are presented for the considered nuclei. Fitted values of the parameters a_1, a_2, c_1 and c_2 are listed with the corresponding fitting details such as rms values σ, total number of data points as well as the scaling parameters β_M and $\hbar^2/2B$ relating the theoretical results with measured units for the energy levels and transition probabilities.

	^{118}Xe	^{120}Xe	^{122}Xe	^{124}Xe	^{126}Xe	^{128}Xe
$R_{4/2}$ exp	2.40	2.47	2.50	2.48	2.42	2.33
$R_{4/2}$ Th	2.40	2.41	2.41	2.39	2.37	2.32
$R^{\beta}_{0/2}$ exp	2.46	2.82	3.47	3.58	3.38	3.57
$R^{\beta}_{0/2}$ Th	2.62	2.93	3.54	3.61	3.33	3.67
$R^{\gamma}_{2/2}$ exp	2.75	2.72	2.55	2.39	2.26	2.19
$R^{\gamma}_{2/2}$ Th	2.49	2.43	2.39	2.36	2.34	2.31
a_1	19.39	33.33	56.86	62.39	54.76	68.49
a_2	10278	10^8	953	464	303.3	9.41
c_1	3.35	2.15	1.65	0.00	0.00	0.00
c_2	0.21	8.84	16.30	16.48	16.26	8.10
N	17	16	14	15	15	12
σ	0.279	0.381	0.413	0.399	0.429	0.382
$\frac{\hbar^2}{2B}$ [keV]	5.195×10^8	4.728×10^{14}	2.979×10^7	1.452×10^7	8.882×10^6	2.695×10^6
β_M	$36.4(19) \times 10^{-5}$	$30.6(40) \times 10^{-7}$	$81.6(29) \times 10^{-5}$	$59.2(88) \times 10^{-5}$	$92.1(24) \times 10^{-5}$	$99.4(51) \times 10^{-5}$

in the Rose's [62] convention for the reduced matrix elements. Taking in consideration that $\mathcal{Q}_{2m} = \frac{4\pi}{\sqrt{15}}\hat{\mathcal{Y}}_{112m}$, the reduced matrix element is ultimately factorized as

$$\begin{aligned}\left\langle \Psi_{n_i L_i \kappa_i} \middle|\middle| T^{E2}_2 \middle|\middle| \Psi_{n_f L_f \kappa_f} \right\rangle &= \frac{3R^2 Ze\beta_M}{\sqrt{15}} I^1_{n_i L_i \kappa_i n_f L_f \kappa_f} \sum_{\substack{\tau_i,\alpha_i \\ \tau_f,\alpha_f}} G^{\kappa_i}_{\tau_i \alpha_i L_i} G^{\kappa_f}_{\tau_f \alpha_f L_f} \\ &\times (\tau_f \alpha_f L_f, 112 || \tau_i \alpha_i L_i) \langle \tau_i ||| \hat{\mathcal{Y}}_1 ||| \tau_f \rangle, \end{aligned} \tag{30}$$

where

$$I^k_{n_i L_i \kappa_i n_f L_f \kappa_f} = \int_0^\infty R_{n_i L_i \kappa_i}(\beta) R_{n_f L_f \kappa_f}(\beta) \beta^{4+k} \left(1 + \frac{a_2}{\beta}\right) d\beta. \tag{31}$$

The reduced matrix element of the spherical harmonic can be extracted from formula (14). In order to follow the selection rules, it can be expressed in a compact form [63,64]

$$\frac{4\pi}{\sqrt{15}} \langle \tau_i ||| \hat{\mathcal{Y}}_1 ||| \tau_f \rangle = \delta_{\tau_i, \tau_f + 1} \sqrt{\frac{\tau_f + 1}{2\tau_f + 5}} + \delta_{\tau_i, \tau_f - 1} \sqrt{\frac{\tau_f + 2}{2\tau_f + 1}}. \tag{32}$$

IV. NUMERICAL APPLICATION

Due to the scaling property of the Bohr model, its numerical applications to actual energy spectra are usually performed in terms of energy ratios. In this way, the model describes effectively the evolution trend of excited energy levels with quantum numbers. This property is invoked here for the determination of the model parameters. This is done by fitting the experimental data of $^{118-128}$Xe nuclei on the ground, γ, and β bands by minimizing the quantity

$$\sigma = \sqrt{\frac{1}{N-1} \sum_{i=1}^{N} \left(\frac{E_{\exp}(i)}{E_{\exp}(2^+_g)} - \frac{E_{Th}(i)}{E_{Th}(2^+_g)} \right)^2}. \tag{33}$$

The absolute theoretical energies are considered in respect to the calculated ground state energy—$E_{Th}(i) = (\epsilon_i - \epsilon_{\text{g.s.}})\hbar^2/2B$. The index "$i$" goes over all N states of ground, β, and γ bands considered in the fit, which are limited to the maximal angular momentum $L = 12$, beyond which the collective experimental spectra of the considered nuclei acquire a single-particle contribution due to quasiparticle pair breaking or alignments. As can be seen, the fit on energy ratios makes the scale factor $\hbar^2/2B$ needless. It is however necessary for the expression of theoretical energy levels in measured units, and is commonly determined by matching the measured energy of the first excited state 2^+_g. The fitted parameters are listed in Table I along with other information such as the number of fitted data points, standard deviation of the fitting procedure, and the deduced scale factor $\hbar^2/2B$, while the resulted theoretical energy spectra are compared with experimental data in Fig. 1. Table I compares also some key spectral observables such as

$$R_{4/2} = \frac{E(4^+_g)}{E(2^+_g)}, \quad R^{\beta}_{0/2} = \frac{E(0^+_\beta)}{E(2^+_g)}, \quad R^{\gamma}_{2/2} = \frac{E(2^+_\gamma)}{E(2^+_g)}. \tag{34}$$

Figure 1 shows a very good agreement with experimental data for all nuclei in the γ and β bands, while the principal source of discrepancy are the high spin states of the ground band. Such a relation between theory and experiment is quite opposite to the usual results of geometrical models, where the ground band is exceptionally well reproduced.

The energy dependence is found to be high for the first two nuclei and suddenly dropping between ^{120}Xe and ^{122}Xe. Afterwards it gradually decreases and finally becoming very small for ^{128}Xe. The very high of a_2 value for ^{120}Xe was fixed

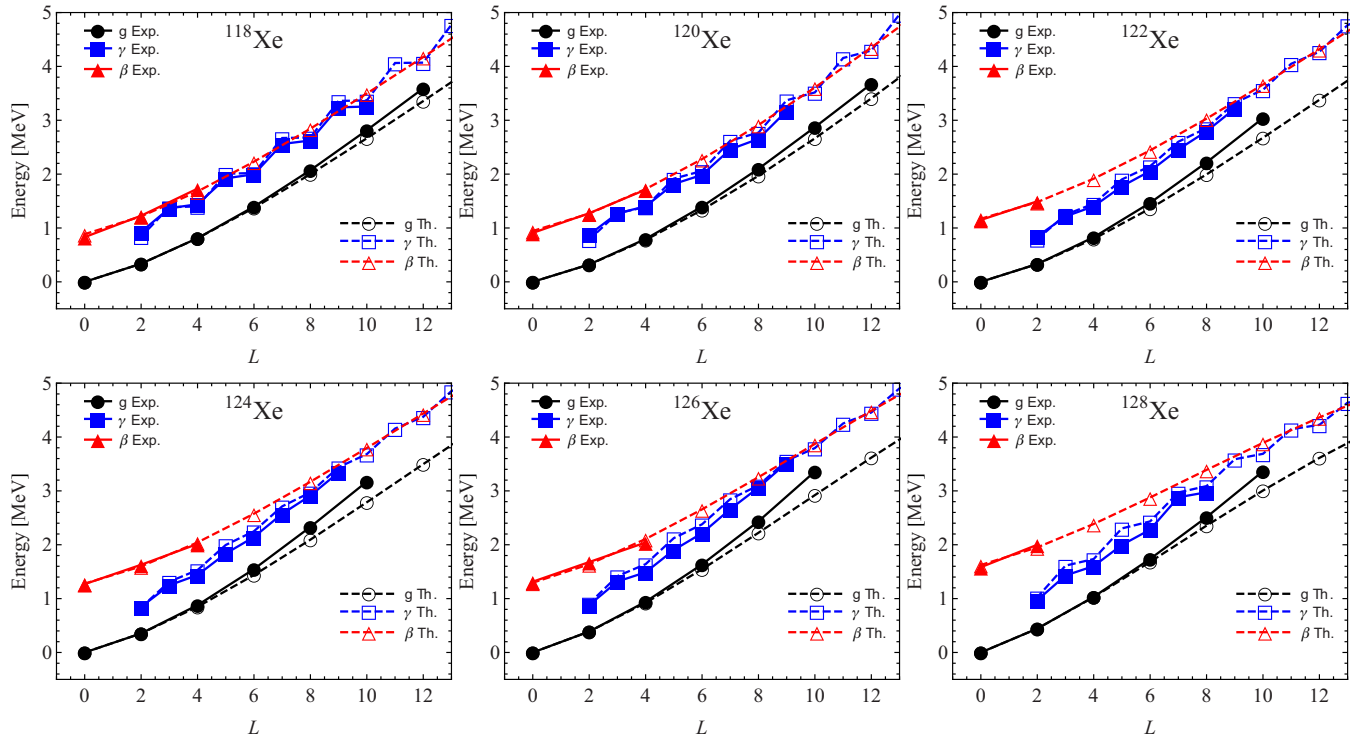

FIG. 1. Excitation energy spectra of ground, γ, and β bands described by Eq. (20) and given in MeV are compared with corresponding experimental levels up to the maximal spin $L = 12^+$ for $^{118-128}$Xe nuclei [67–72]. The experimental data point for the 7^+_γ state of ^{128}Xe is only tentative and was not considered in the fitting procedure.

such that for its larger values, the rms value would vary only in its fifth decimal. This is due to the saturation properties of the model in the asymptotic regime of parameter a_2. Indeed, in the large a_2 limit, the energy (20) can be approximated as

$$\epsilon^{\text{asymp}}_{nL\kappa} = -\frac{1}{a_2} + \frac{2}{a_2^{3/2}}(n + p_{L\kappa} + 2). \tag{35}$$

Therefore, parameter a_2 becomes a simple scaling factor for the excitation energies and the fitted energy ratios lose their dependence on it. The saturation of energy depends on the state, and is attained for the whole considered spectrum at quiet high values of a_2. In this context, the choice of a_2 for ^{120}Xe seems arbitrary, provided a similarly high value for $\hbar^2/2B$ is chosen to reproduce the measured data. However, although the scaling property of a_2 is also reflected in the wave-function, the scalar products are performed on unscaled variable β. Therefore a choice of a_2 is still needed and for numerical considerations mentioned above a finite value is chosen.

Comparing to other geometrical model applications on the same nuclei, the additional parameters included in the present calculations lead to a relatively low gain in rms values. As it happens, the agreement with experiment is improved the most for the lightest Xe isotopes, which, judging by the fitted parameters, exhibit a very accentuated energy dependence of the β potential. The agreement with experiment is however improved qualitatively, in particular for the γ and β band states. This is a good example of the dangers involved in blind fits on experimental data [65]. More precisely, although the overall agreement of various geometrical models with experimental data is good for many of the nuclei considered here, and subjective spectral observables are sufficiently well reproduced, some qualitative features are ignored. For example, the γ band staggering behavior is completely overlooked through drastic approximations such as the γ-unstable idealization [12,13,16] or the rigid triaxiality [14], while the rotational sequence of the β band is often traded for an approximative matching of the β band-head state. The success of the present description of the γ band evolution with spin can be better traced through the measure of the γ band staggering pattern proposed in Ref. [66] and defined as

$$S(L) = \frac{E(L) - 2E(L-1) + E(L-2)}{E(2^+_g)}. \tag{36}$$

This quantity is visualized as a function of angular momentum for each nucleus in Fig. 2. The agreement with experiment is obvious, as well as the fact that the staggering phasing is consistent with γ-softness or dynamical triaxiality rather than rigid triaxiality [2]. One can also observe that the staggering measure $|S(L)|$ evolves from an increasing function in ^{118,120}Xe to a decreasing one in the rest of the nuclei in what concerns both experimental data and theoretical predictions. The latter changes back to an increasing function around $L = 8$ only in ^{122,124,126}Xe. Such a behavior is out of the guidelines presented for the cornerstone geometrical models [2], whose function $|S(L)|$ is constant or increasing with L. The change of the γ band staggering throughout the considered nuclei can be correlated with the shapes of

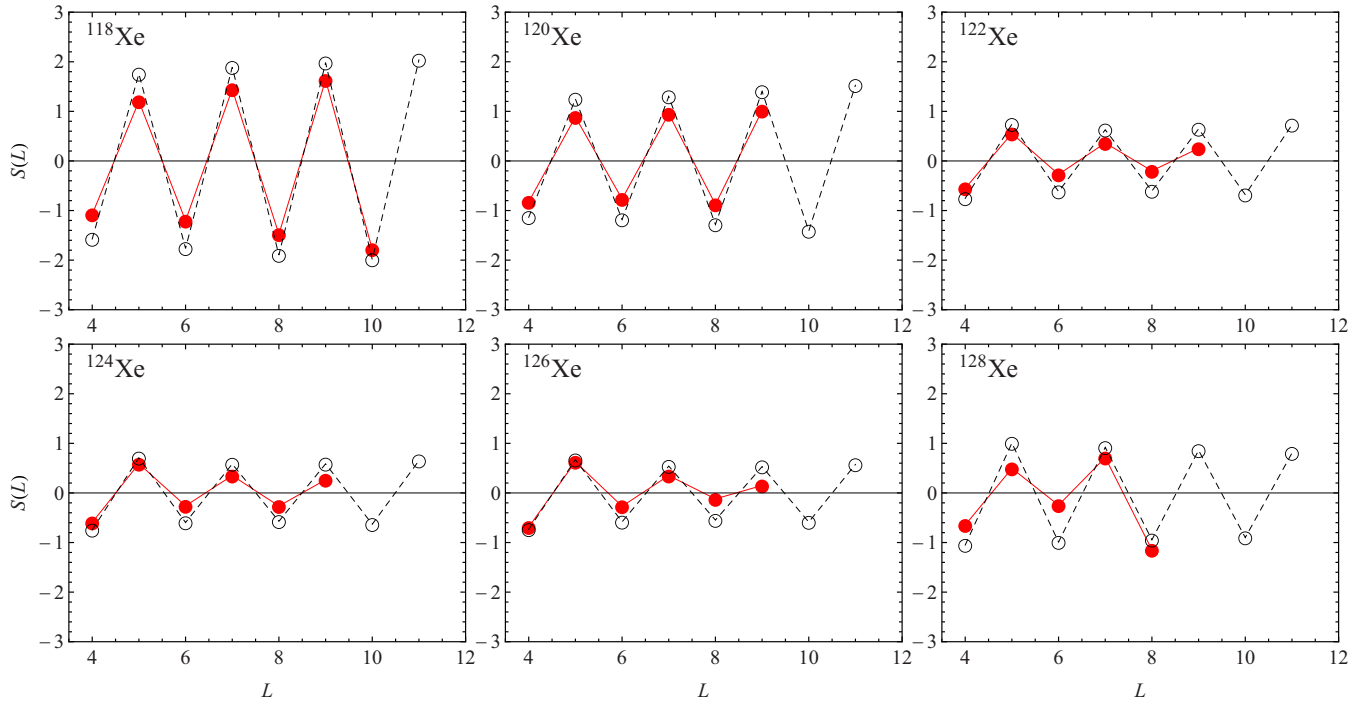

FIG. 2. Experimental and theoretical γ band staggering $S(L)$ given by Eq. (36) is visualized as a function of angular momentum for the considered $^{118-128}$Xe nuclei. The experimental data point for the 7^+_γ state of ^{128}Xe is only tentative.

the fitted γ potential $w(\gamma)$ depicted in Fig. 3. Checking this picture, one can now see that the large $|S(L)|$ values for ^{118}Xe are due to a very shallow axially symmetric potential which leads to approximate γ-unstable conditions [50]. The next nucleus, ^{120}Xe, already acquires a triaxial minimum in its γ potential. However, the shallowness of its minimum and the fact that its oblate part is higher than the prolate one, lead to a similar behavior of its associated excitations. The next three nuclei exhibit very deep and symmetrical triaxial minima. While the triaxial minimum for ^{128}Xe is considerably shallower, pointing to a more γ-unstable character consistent with an increased $|S(L)|$ function. The $S(L)$ function for ^{122,124,126}Xe nuclei with the deepest triaxial minima in their γ potential tends to a constant value at high spin states. By Ref. [2], such a behavior would correspond to γ-stable axially symmetric conditions. It must be noted here that the excellent

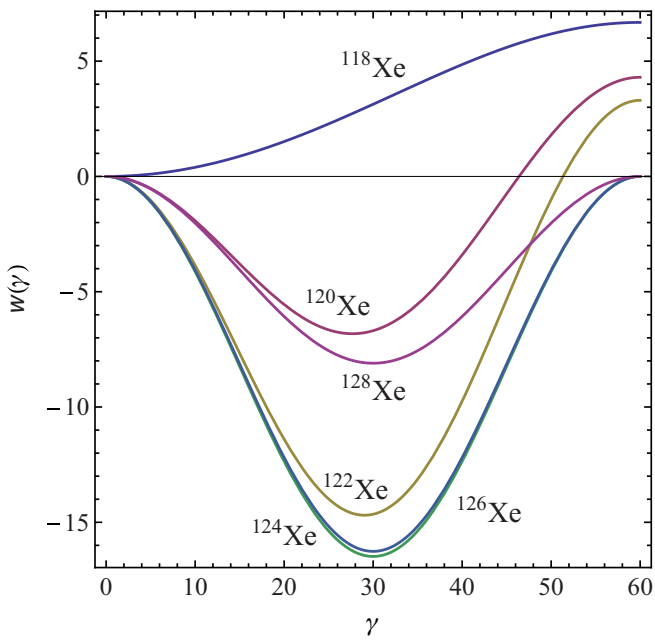

FIG. 3. The evolution of the γ potential defined by Eq. (7) with fitted parameters c_1 and c_2, along the isotopic chain $^{118-128}$Xe.

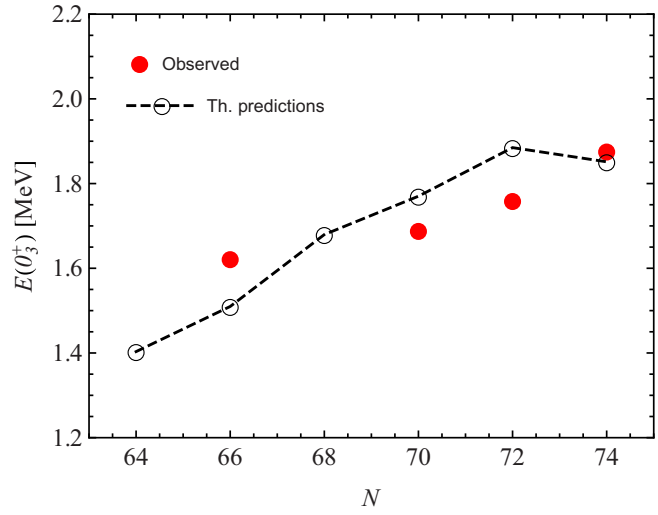

FIG. 4. Theoretical predictions of the three phonon 0^+ state are compared with the observed energy levels 0^+_3 [68,70–72].

TABLE II. Theoretical results (second row) for the in-band quadrupole transition probabilities compared with experimental data (first row) [27,67–70,72]. Values are given in W.u.

Transition	^{118}Xe	^{120}Xe	^{122}Xe	^{124}Xe	^{126}Xe	^{128}Xe
$2_g \rightarrow 0_g$	84(4)	101(5)	78(4)	57.8(15)	41.0(13)	48(11)
	55(6)	43(11)	72(5)	25(7)	39(2)	31(3)
$4_g \rightarrow 2_g$	93.1(15)	117(8)	114(6)	67.6(19)	71(7)	62(3)
	93(10)	68(18)	114(8)	40(12)	63(3)	49(5)
$6_g \rightarrow 4_g$	74(19)	118(18)	110(40)	88(8)	84(11)	61(3)
	130(14)	93(24)	153(11)	54(16)	86(4)	67(7)
$8_g \rightarrow 6_g$	41(15)	97(17)	80(50)	66(21)		95(11)
	174(18)	120(31)	195(14)	68(20)	112(6)	87(9)
$10_g \rightarrow 8_g$	>61	92(15)	120(50)	21(3)		
	227(24)	150(39)	243(17)	86(25)	144(7)	113(11)
$12_g \rightarrow 10_g$		83(13)				
	290(31)	185(48)	300(21)	106(32)	183(9)	145(15)
$3_\gamma \rightarrow 2_\gamma$				9(4)	56(6)	210(30)
	94(10)	74(19)	128(9)	45(13)	72(4)	52(5)
$4_\gamma \rightarrow 2_\gamma$				69(25)	36(4)	27.7(18)
	69(7)	45(12)	70(5)	24(7)	39(2)	32(3)
$5_\gamma \rightarrow 3_\gamma$				37(5)		
	92(10)	61(16)	98(7)	34(10)	56(3)	45(5)
$5_\gamma \rightarrow 4_\gamma$				35(6)		
	42(4)	34(9)	61(4)	22(6)	36(2)	24(2)
$6_\gamma \rightarrow 4_\gamma$						
	121(13)	79(21)	123(9)	43(13)	71(4)	57(6)
$7_\gamma \rightarrow 5_\gamma$		140(80)				
	156(17)	101(26)	160(11)	56(17)	95(5)	76(8)
$7_\gamma \rightarrow 6_\gamma$						
	28(3)	22(6)	41(3)	15(4)	25(1)	16(2)
$8_\gamma \rightarrow 6_\gamma$						
	175(18)	113(29)	180(13)	63(19)	107(5)	85(9)
$9_\gamma \rightarrow 7_\gamma$		150(50)				
	222(23)	139(36)	222(16)	79(23)	136(7)	109(11)
$9_\gamma \rightarrow 8_\gamma$						
	21(2)	16(4)	31(2)	11(3)	19(1)	13(1)
$2_\beta \rightarrow 0_\beta$				62(36)[a]	38(9)	
	78(8)	56(15)	103(7)	37(11)	60(3)	53(5)
$4_\beta \rightarrow 2_\beta$						
	124(13)	88(23)	158(11)	57(17)	93(5)	82(8)

[a]Data taken from Ref. [26] and not considered in the fitting procedure.

reproduction of staggering evolution is due to the combined effect of the chosen γ potential and the energy dependence of the β potential. The average γ deformation is however solely given by the γ-angular degrees of freedom, and its value around $\gamma = 30^\circ$ does not vary substantially between different angular momentum states [49,50].

The validity of the triaxial features evidenced above, can be checked by investigating the available experimental data on the energy of the 0_3^+ state for the considered nuclei. In the present formalism, this state would correspond to the three-phonon band-head. In Fig. 4, one can see that the model predictions reproduce with good accuracy the energy of the 0_3^+ state for ^{120}Xe and ^{124,126,128}Xe nuclei, and its overall increasing trend with neutron number. The present interpretation of these states is in contradiction with recent theoretical descriptions based on IBM [26,27] or ACM [17] of the heaviest three nuclei. These studies identify the first excited 0_2^+ state as the band-head of the $K = 0$ three phonon band, based on the O(5) spectral grouping and selection rules for transition probabilities. Nevertheless, the high values of the reported quadrupole transitions connecting the 0_2^+ state with ground and γ band 2^+ states in the ^{124,126,128}Xe nuclei [11,26,27], which is the main criterion for the assignment of 0_2^+ state to the three-phonon band, have big uncertainties due to the approximate degeneracy with 3_1^+ states and do not appear in the updated data evaluations. From our calculation, the correct reproduction of the γ band infers a much higher position of the three-phonon 0^+ state. Also, due to the particularity of the β excitations stemming from energy dependence, the transition probabilities connecting the β states with ground band states are extremely well described and do not contradict even the older data values. There is however a striking inconsistency related to the transition $0_2^+ \rightarrow 2_2^+$ whose experimentally deduced rate is quite high, while the present model essentially

TABLE III. Theoretical results (second row) for the interband quadrupole transition probabilities compared with experimental data (first row) [27,67–70,72]. Values are given in W.u.

Transition	^{118}Xe	^{120}Xe	^{122}Xe	^{124}Xe	^{126}Xe	^{128}Xe
$2_\gamma \rightarrow 0_g$				0.71(13)	0.63(7)	0.76(5)
	0.77(8)	0.20(5)	0.16(1)	≈0	≈0	≈0
$2_\gamma \rightarrow 2_g$				32(6)	43(3)	57(4)
	82(9)	66(17)	112(8)	40(12)	62(3)	49(5)
$3_\gamma \rightarrow 2_g$				0.79(15)	0.90(23)	3.3(5)
	1.33(14)	6.35(9)	0.28(2)	≈0	≈0	≈0
$3_\gamma \rightarrow 4_g$				26(12)[a]	⩽22.1(13)	72(10)
	36(4)	29(8)	53(4)	19(6)	30(2)	21(2)
$4_\gamma \rightarrow 2_g$				0.06(1)[a]	0.40(8)	
	0.011(1)	≈0	≈0	≈0	≈0	≈0
$4_\gamma \rightarrow 4_g$				34(13)	28(4)	28(3)
	57(6)	40(10)	61(4)	21(6)	35(2)	29(3)
$5_\gamma \rightarrow 4_g$				0.5(3)		
	0.52(6)	0.11(3)	0.073(5)	≈0	≈0	≈0
$0_\beta \rightarrow 2_g$				13.2(31)[a]	5.9(9)	3.7(6)[b]
	50(5)	31(8)	44(3)	15(4)	27(1)	18(2)
$2_\beta \rightarrow 0_g$				0.32(5)[a]	0.063(14)	
	1.68(18)	1.42(37)	1.92(13)	0.60(18)	0.84(4)	0.34(3)
$2_\beta \rightarrow 2_g$				0.61(7)[a]	⩽0.10(2)	
	0.89(9)	0.19(5)	0.12(1)	≈0	≈0	≈0
$2_\beta \rightarrow 4_g$				5.55(79)[a]	0.96(4)	
	35(4)	21(5)	30(2)	10(3)	19(1)	14(1)
$0_\beta \rightarrow 2_\gamma$				87(21)[a]	64(9)	52.8(76)[b]
	1.43(15)	0.27(7)	0.18(1)	≈0	≈0	≈0
$2_\beta \rightarrow 2_\gamma$				3.54(71)[a]	⩽1.9(4)	
	18(2)	11(3)	16(1)	6(2)	10(1)	8(1)
$2_\beta \rightarrow 3_\gamma$					⩽21(4)	
	0.84(9)	0.15(4)	0.10(1)	≈0	≈0	≈0
$2_\beta \rightarrow 4_\gamma$						
	0.0087(9)	≈0	≈0	≈0	≈0	≈

[a]Data taken from Ref. [26].
[b]Data taken from Ref. [11].

forbids it. This can be seen in Tables II and III, where the available experimental data for transition probabilities are compared with theoretical predictions. The latter values are calculated with the wave-functions determined from the fitting procedure, with the additional scaling parameter β_M fitted to reproduce the experimental data only for the in-band transitions which have measured values usually of the same order of magnitude. The fitting is made by including also the errors, which are substantial:

$$\sigma_{E2} = \sqrt{\frac{1}{N_{E2}} \sum_{i=1}^{N_{E2}} \left(\frac{B^i_{\rm exp}(E2) - B^i_{Th}(E2;\beta_M)}{\sigma^i_{E2}} \right)^2}. \quad (37)$$

N_{E2} is the number of data points considered in the fitting procedure, while σ^i_{E2} is the absolute error of the experimental $E2$ transition probability data point $B^i_{\rm exp}(E2)$. The inclusion of errors is essential in making valid theoretical predictions. The obtained scaling parameter β_M is listed in Table I with its associated theoretical error. As the fit of the scaling parameter was made on the in-band transitions, the associated experimental data is overall well reproduced by the theory. Special mention deserves the very good theoretical description of the in band transitions for ^{126}Xe and ^{128}Xe. Surprisingly, the data available on inter-band transitions only for the ^{124,126,128}Xe are also in a very good agreement with the extrapolated theoretical values, with the exception of the transition $0^+_{2(\beta)} \rightarrow 2^+_{2(\gamma)}$ discussed above.

With the use of the scaling parameters, one can draw the total potential for the ground state in terms of the quadrupole deformation β_2 and the triaxial deformation. This is done in Fig. 5, from where one can observe the evolution of the triaxial deformation as well as the softness of the quadrupole deformation through the considered Xe isotopes. As was mention in connection to the γ potential, the triaxiality establishes itself quite suddenly starting from ^{120}Xe nucleus with $\gamma = 26.67^\circ$. The equilibrium triaxiality rapidly increases to 30° in the last three nuclei. The evolution of the quadrupole deformation associated with the ground state potential minimum, is more erratic. Indeed, the first nuclei have similar deformation around $\beta_2 = 0.13$, and then there is a consistent increase in deformation up to $\beta_2 = 0.18$ in ^{122}Xe and then a similarly abrupt decrease to $\beta_2 = 0.11$. After that, the deformation stabilizes to almost the same deformation as in the first two

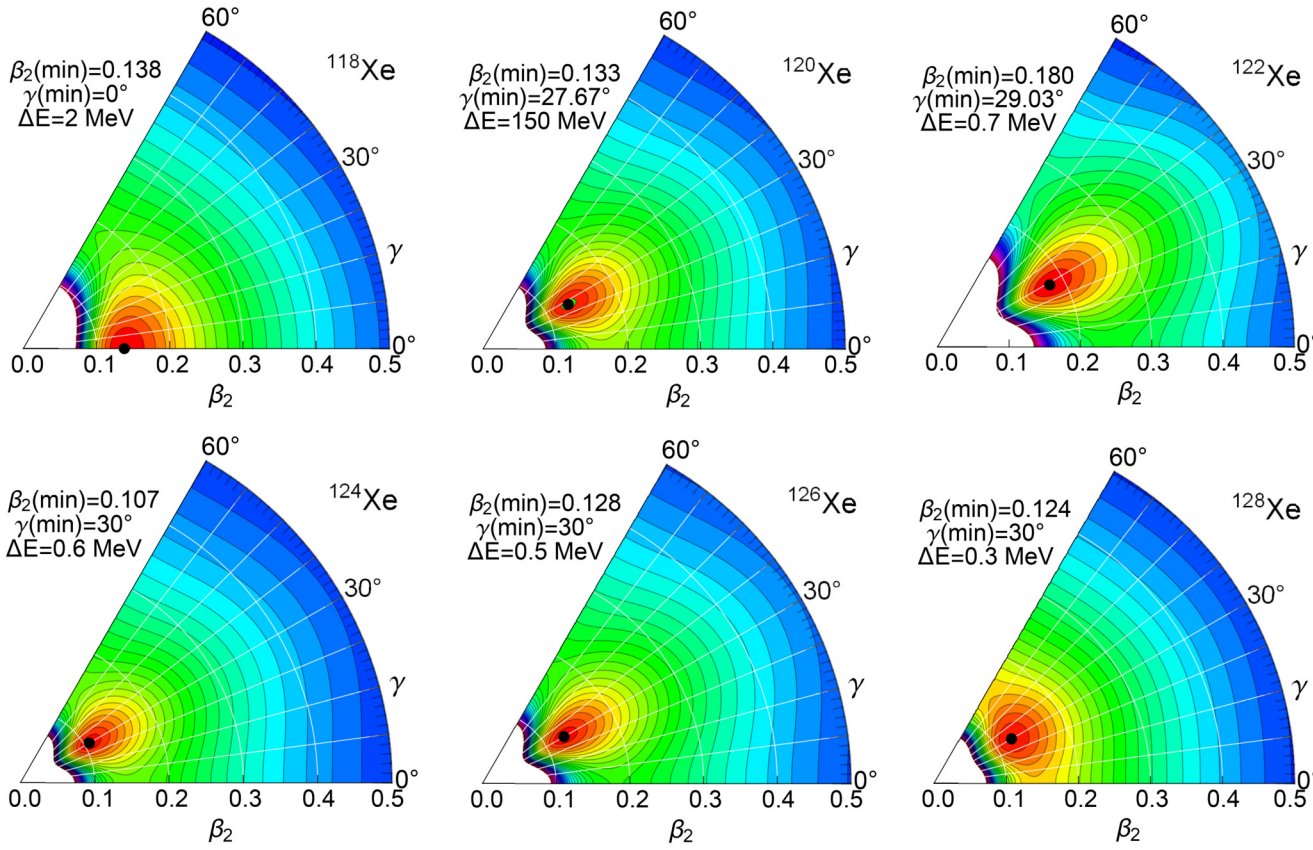

FIG. 5. Total potential U from Eq. (1) for the ground state as a function of the quadrupole deformation $\beta_2 = \beta_M\beta$ and triaxiality measure γ. The contour step is given for each nucleus by ΔE.

nuclei. Note however that the equilibrium quadrupole deformation associated with the ground state potential minimum is by 50% smaller than its associated average quadrupole deformation due to the very anharmonic character of the potential. As a matter of fact, these averages are in good agreement with the quadrupole deformation values extracted from experiment [73]. Indeed, Fig. 6 shows that the overall trend of experimentally determined deformation values is sufficiently well reproduced. The same figure shows also the theoretical quadrupole deformation in the 0^+_β state. Except ^{120}Xe nucleus, in all cases the deformation of the excited state is higher with approximately the same factor. The departure is larger for ^{128}Xe whose energy dependence is the weakest among all considered nuclei. The excepted ^{120}Xe nucleus exhibits actually a suppression of deformation from the excited state in respect to the ground state. This behavior was reported before in Ref. [43] in connection with the energy dependence of a Davidson potential in axially symmetric limit.

The dynamical properties of the considered nuclei in each state are more obvious from the correspondence between the shape of an effective potential which includes the centrifugal contribution and the associated density probability distribution $\rho = |\Psi_{nLK}|^2(1 + a_2/\beta)\beta^4$. Such an effective potential is obtained by a change of function $R(\beta) = f(\beta)/\beta^2$ in Eq. (5), which leads to

$$V_{\rm eff} = \frac{\hbar^2}{2B}\left(\frac{2 + W_{LK} + a_1}{\beta^2} - \frac{1 + a_2\epsilon_{nLK}}{\beta}\right). \qquad (38)$$

Both effective potential, and the density probability distribution can be transformed to depend on the quadrupole deformation by using the change of variable $\beta_2 = \beta_M\beta$. The two

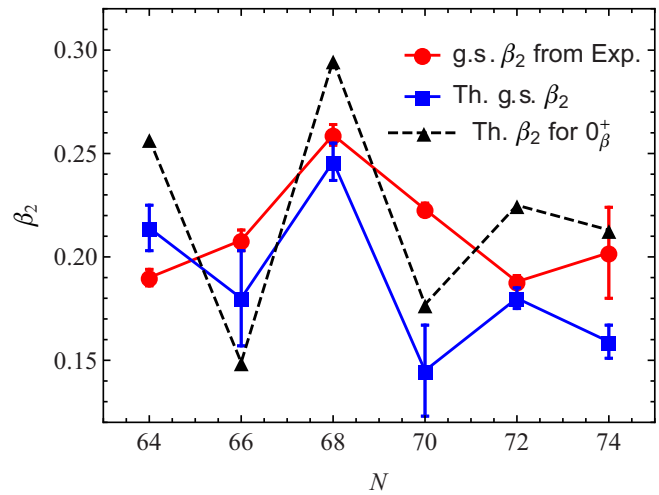

FIG. 6. Theoretical predictions for the ground state quadrupole deformation are compared with values extracted from experiment [73] and with the similarly calculated 0^+_β state quadrupole deformation. The theoretical error bars are presented only for the ground state deformation, with those corresponding to the excited states having the same proportion in respect to their absolute values.

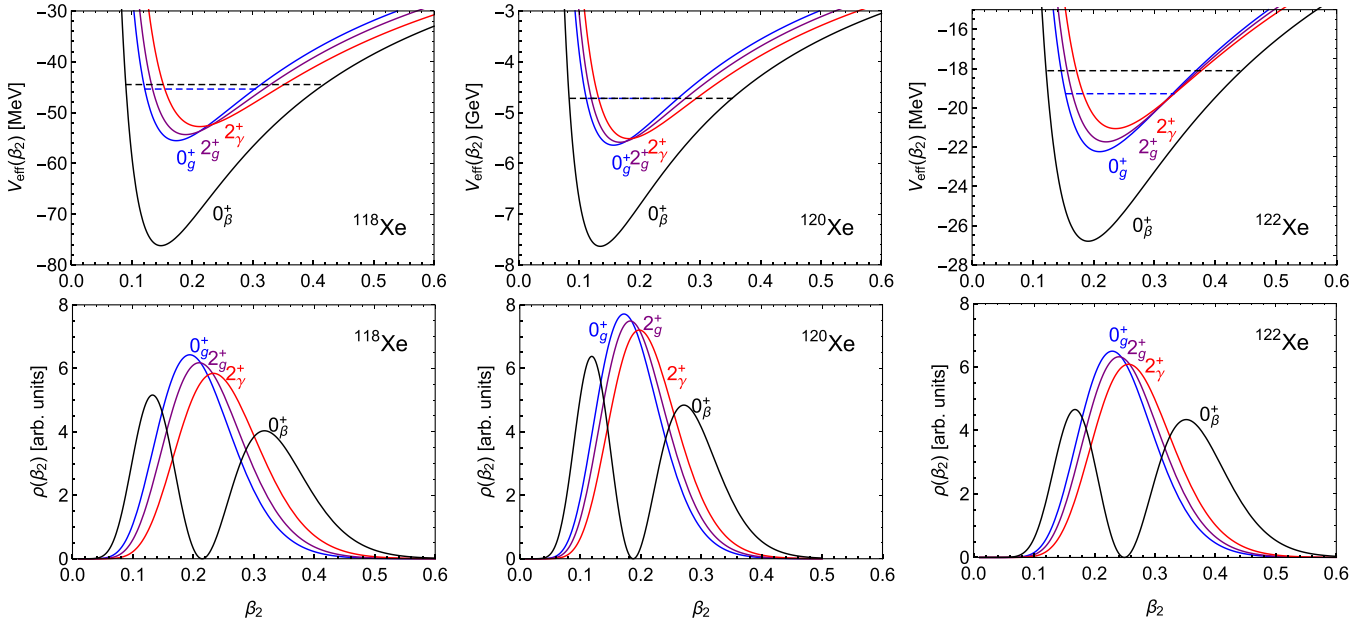

FIG. 7. The effective potential for the β_2 deformation variable and the associated probability distribution for the 0^+_g, 2^+_g, 2^+_γ, and 0^+_β states of the ^{118,120,122}Xe nuclei. The corresponding ground and β excited 0^+ states are also shown by dashed lines.

quantities are shown for the 0^+_g, 2^+_g, 2^+_γ, and 0^+_β states of each considered nucleus in Figs. 7 and 8, where the correspondence between them becomes obvious. Whenever the energy dependence of the potential is strong, the effective potential for the 0^+_β state is much deeper than those associated with rotational excitations and even the ground state, but with a similar asymptotic behavior. This effect is reflected in the relative height of the two peaks associated with the density probability distribution for the 0^+_β state. Indeed, a very strong energy dependence induces a larger probability for the low deformation turning point as it happens in ^{118}Xe and ^{120}Xe. While mild energy dependence obtained for ^{122,124,126}Xe equalizes the probability of the two deformation turning points associated with the β vibration. In this latter case, one can say that the β variable behaves as in a one-dimensional harmonic oscillator. The low energy dependence found for ^{128}Xe corresponds to a usual behavior of the β excited state which probabilistically favors the high deformation turning point. Although for this nucleus the slope of the energy dependence is small, the resulted effective potential for the 0^+_β excited state is still slightly deeper than the effective potential for the ground state. The effective potentials of Figs. 7 and 8 seem

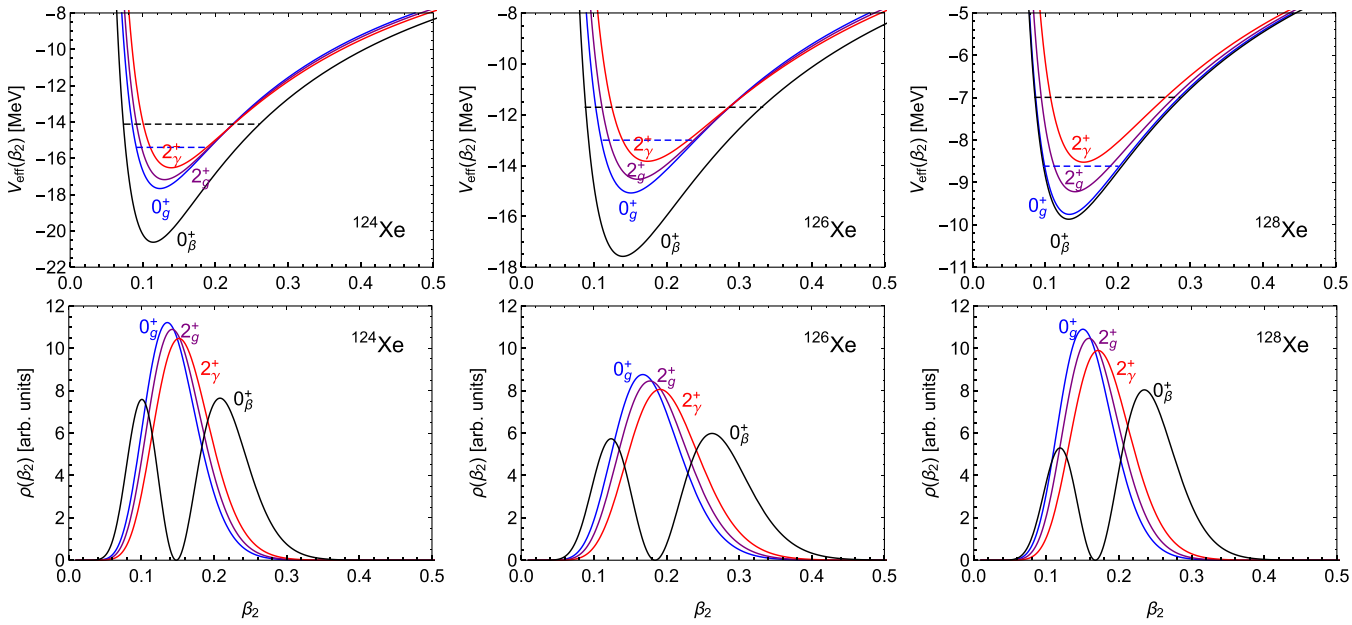

FIG. 8. Same as in Fig. 7 but for the ^{124,126,128}Xe nuclei.

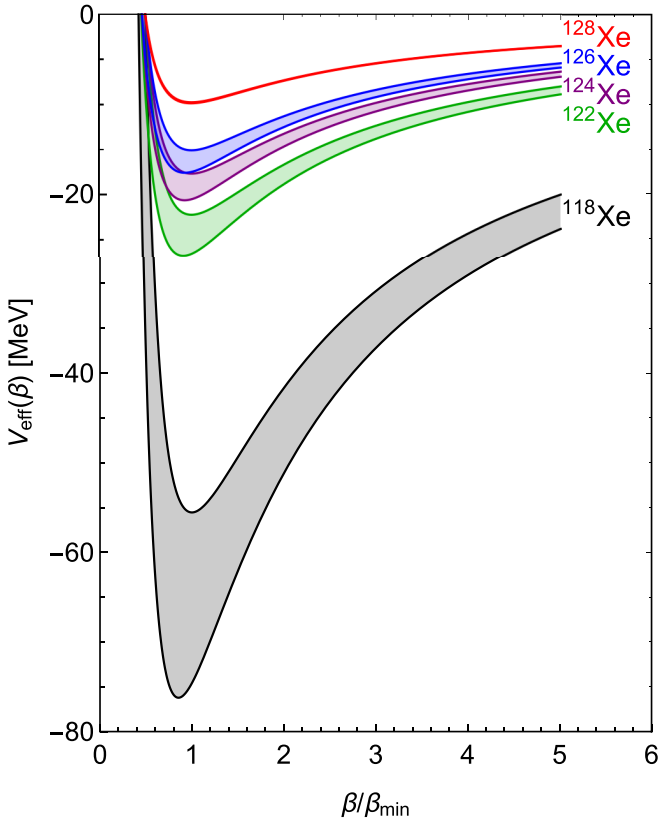

FIG. 9. Variation of the effective potential for $^{118,122-128}$Xe nuclei between ground state and the first β excited state. Note that the ground state effective potential is the upper curve.

to have similar shapes, but are nevertheless differently scaled. Indeed, the potentials depicted in Figs. 5, 7, and 8 have significant variation with quadrupole deformation only in large energy intervals of many MeV units, but the actual spectra are very compressed in the relevant interval of excitation energies.

In order to observe the actual changes in the effective potentials between nuclei and also between states, one plotted them within the same scale in Fig. 9 and as a function of a β deformation variable normalized to the position of the ground state effective potential minimum $\beta_{\rm min}$. Such a representation demonstrates the evolution with mass number of the effective potential from very sharp minimum with strong state-dependence to a shallow minimum with an approximate state-independence. The ^{120}Xe nucleus falls out from this trend because, in the same scale of Fig. 9, it will show a very deep minimum with large energy variance between states. However, taking it into account, one observes that the evolution of the effective potential and its state-dependence is consistent with the change of the neutron valence space [13]. As it happens, ^{120}Xe is just at the neutron midshell $N = 66$. Its deepest potential minimum is then consistent with larger shape fluctuations, while its sensitive energy-dependence is a consequence of the maximal valence space which allows more substantial microscopic changes between collective states.

In what concerns the behavior of the rotationally excited states, their effective potentials and associated probability distributions are quite stabilized, with a slightly wider spread for ^{118}Xe and ^{120}Xe, whose γ deformation is more prolate-like. It must be mentioned here that the theoretical errors for the quadrupole deformation used in Figs. 5, 7, 8, and 9 were discarded for the sake of a clear presentation.

The analysis on the evolution with neutron number of both triaxiality and the shape state dependence point to the fact that a transition takes place in between ^{120}Xe and ^{122}Xe nuclei from axial shapes with β excitations favoring low quadrupole deformation towards triaxial shapes with β excitations favoring higher deformation. This transition coincides also with the evolution of the decay stability along the Xe isotopes [73], which changes from very short-lived ^{118}Xe to the stable nuclei ^{124,126,128}Xe. The critical role of ^{120,122}Xe is enforced in the present study by the strongest energy dependence for ^{120}Xe and respectively the highest quadrupole deformation obtained for ^{122}Xe. The latter is also experimentally observed. Moreover the lowest-lying γ band-head state is observed and calculated for ^{122}Xe nucleus.

The model calculations can be easily transposed to a Davidson potential in the β variable. However, the fits performed with an energy-dependent Kratzer potential were found to be significantly better than those for the Davidson potential with an energy-dependent harmonic term.

V. CONCLUSIONS

A phenomenological Bohr model with an exactly separable collective potential allowing axial and triaxial minima of varying depth and softness is proposed in connection with a non-local formalism for the β excitations. The energy dependence of the β excitations, like the formalisms involving deformation dependent mass terms [12,13], shows a superior ability in treating β excited states. While the adopted γ potential is sufficiently versatile to reproduce truthfully the majority of spectral behaviours of the γ band, the β variable part of the formalism is fully analytic, but the equation involving the γ-angular degrees of freedom is diagonalized in a basis of SO(5) spherical harmonics. The model is applied for the description of energy spectra and $E2$ transition probabilities of the $^{118-128}$Xe nuclei, which is achieved with high accuracy. The model parameters deduced from experimental data are used to draw conclusion regarding the dynamical features of the considered nuclei in connection to their deformation. The main result is the identification of the transition from axial to triaxial shapes happening at ^{120}Xe nucleus, and maintaining to the maximum value of $\gamma = 30^\circ$ up to the last considered nucleus ^{128}Xe. Additionally, the energy dependence of the β excitations shows a change in the most probable deformation turning point in the oscillation of the β shape variable. This is happening around ^{122}Xe nucleus, although the strongest energy dependence is reported for ^{120}Xe. However, this strong energy dependence is vividly and uniquely reflected in the decrease of the β excited state quadrupole deformation in respect to the ground state in ^{120}Xe.

The present study offers also an alternative interpretation of the excited 0^+ states in the considered Xe nuclei, which must be further validated by more precise measurements of interband $E2$ transition probabilities.

ACKNOWLEDGMENTS

This work was supported by a grant of Ministry of Research and Innovation, CNCS-UEFISCDI, Project No. PN-III-P1-1.1-TE-2016-0268 within PNCDI III.

[1] C. Bihari, M. Singh, Y. Singh, A. K. Varshney, K. K. Gupta, and D. K. Gupta, Phys. Scr. **77**, 055201 (2008).
[2] E. A. McCutchan, D. Bonatsos, N. V. Zamfir, and R. F. Casten, Phys. Rev. C **76**, 024306 (2007).
[3] Q. B. Chen, S. Frauendorf, and C. M. Petrache, Phys. Rev. C **100**, 061301(R) (2019).
[4] Y. K. Wang, F. Q. Chen, and P. W. Zhao, Phys. Lett. B **802**, 135246 (2020).
[5] S. Biswas *et al.*, Eur. Phys. J. A **55**, 159 (2019).
[6] J. T. Matta, U. Garg, W. Li, S. Frauendorf, A. D. Ayangeakaa, D. Patel *et al.*, Phys. Rev. Lett. **114**, 082501 (2015).
[7] N. Sensharma *et al.*, Phys. Lett. B **792**, 170 (2019).
[8] B. W. Xiong and Y. Y. Wang, At. Data Nucl. Data Tables **125**, 193 (2019).
[9] P. Cejnar, J. Jolie, and R. F. Casten, Rev. Mod. Phys. **82**, 2155 (2010).
[10] R. F. Casten, Nat. Phys. **2**, 811 (2006).
[11] L. Coquard, N. Pietralla, T. Ahn, G. Rainovski, L. Bettermann, M. P. Carpenter, R. V. F. Janssens, J. Leske, C. J. Lister, O. Möller, W. Rother, V. Werner, and S. Zhu, Phys. Rev. C **80**, 061304(R) (2009).
[12] D. Bonatsos, P. E. Georgoudis, D. Lenis, N. Minkov, and C. Quesne, Phys. Rev. C **83**, 044321 (2011).
[13] D. Bonatsos, P. E. Georgoudis, N. Minkov, D. Petrellis, and C. Quesne, Phys. Rev. C **88**, 034316 (2013).
[14] P. Buganu and R. Budaca, Phys. Rev. C **91**, 014306 (2015).
[15] M. Chabab, A. Lahbas, and M. Oulne, Eur. Phys. J. A **51**, 131 (2015).
[16] M. Chabab, A. El Batoul, A. Lahbas, and M. Oulne, Nucl. Phys. A **953**, 158 (2016).
[17] M. Abolghasem, B. Cuxac, G. Thiamova, and P. Alexa, Phys. Scr. **95**, 034010 (2020).
[18] L. Próchniak, P. Quentin, D. Samsoen, and J. Libert, Nucl. Phys. A **730**, 59 (2004).
[19] Z. P. Li, T. Nikšić, D. Vretenar, and J. Meng, Phys. Rev. C **81**, 034316 (2010).
[20] N. Hinohara, Z. P. Li, T. Nakatsukasa, T. Nikšić, and D. Vretenar, Phys. Rev. C **85**, 024323 (2012).
[21] L. Próchniak, Phys. Scr. **90**, 114005 (2015).
[22] A. Bohr, Mat. Fys. Medd. K. Dan. Vidensk. Selsk. **26**, 14 (1952).
[23] A. Bohr and B. R. Mottelson, Mat. Fys. Medd. Dan. Vidensk. Selsk. **27**, 16 (1953).
[24] B. Sorgunlu and P. Van Isacker, Nucl. Phys. A **808**, 27 (2008).
[25] A. D. Efimov and V. M. Mikhajlov, Bull. Russ. Acad. Sci. Phys. **82**, 1266 (2018).
[26] G. Rainovski, N. Pietralla, T. Ahn, L. Coquard, C. J. Lister, R. V. F. Janssens, M. P. Carpenter, S. Zhu, L. Bettermann, J. Jolie, W. Rother, R. V. Jolos, and V. Werner, Phys. Lett. B **683**, 11 (2010).
[27] L. Coquard, G. Rainovski, N. Pietralla, T. Ahn, L. Bettermann, M. P. Carpenter, R. V. F. Janssens, J. Leske, C. J. Lister, O. Möller, T. Möller, W. Rother, V. Werner, and S. Zhu, Phys. Rev. C **83**, 044318 (2011).
[28] J. B. Gupta, Nucl. Phys. A **927**, 53 (2014).
[29] J. N. Orce *et al.*, Phys. Rev. C **74**, 034318 (2006).
[30] L. M. Robledo, R. R. Rodríguez-Guzmań, and P. Sarriguren, Phys. Rev. C **78**, 034314 (2008).
[31] X.-f. Meng, F.-r. Wang, Y.-a. Luo, F. Pan, and J. P. Draayer, Phys. Rev. C **77**, 047304 (2008).
[32] K. Higashiyama and N. Yoshinaga, Phys. Rev. C **83**, 034321 (2011).
[33] R. F. Casten and P. Von Brentano, Phys. Lett. B **152**, 22 (1985).
[34] S. Singh, R. Chandra, P. K. Rath, P. K. Raina, and J. G. Hirsch, Eur. Phys. J. A **33**, 375 (2007).
[35] N. Ackerman *et al.*, Phys. Rev. Lett. **107**, 212501 (2011).
[36] E. Aprile *et al.*, Nat. Phys. **568**, 532 (2019).
[37] V. I. Tretyak and Yu. G. Zdesenko, At. Data Nucl. Data Tables **80**, 83 (2002).
[38] D. J. Rowe, T. A. Welsh, and M. A. Caprio, Phys. Rev. C **79**, 054304 (2009).
[39] D. J. Rowe and J. L. Wood, *Fundamentals of Nuclear Models: Foundational Models* (World Scientific, Singapore, 2010).
[40] T. A. Welsh and D. J. Rowe, Comput. Phys. Commun. **200**, 220 (2016).
[41] R. Budaca, Phys. Lett. B **751**, 39 (2015).
[42] R. Budaca, Eur. Phys. J. A **52**, 314 (2016).
[43] A. I. Budaca and R. Budaca, Phys. Scr. **92**, 084001 (2017).
[44] A. I. Budaca and R. Budaca, Eur. Phys. J. Plus **134**, 145 (2019).
[45] L. Wilets and M. Jean, Phys. Rev. **102**, 788 (1956).
[46] L. Fortunato, Phys. Rev. C **70**, 011302(R) (2004).
[47] D. Bonatsos, D. Lenis, E. A. McCutchan, D. Petrellis, and I. Yigitoglu, Phys. Lett. B **649**, 394 (2007).
[48] F. Iachello, Phys. Rev. Lett. **91**, 132502 (2003).
[49] M. A. Caprio, Phys. Lett. B **672**, 396 (2009).
[50] M. A. Caprio, Phys. Rev. C **83**, 064309 (2011).
[51] D. J. Rowe, P. S. Turner, and J. Repka, J. Math. Phys. **45**, 2761 (2004).
[52] G. Rakavy, Nucl. Phys. **4**, 289 (1957).
[53] D. R. Bes, Nucl. Phys. **10**, 373 (1959).
[54] M. Abramowitz and I. A. Stegun, *Handbook of Mathematical Functions with Formulas, Graphs, and Mathematical Tables* (Dover, New York, 1972).
[55] A. Kratzer, Z. Phys. **3**, 289 (1920).
[56] L. Fortunato and A. Vitturi, J. Phys. G: Nucl. Part. Phys. **29**, 1341 (2003).
[57] J. Formanek, R. J. Lombard, and J. Mares, Czech. J. Phys. **54**, 289 (2004).
[58] D. Bonatsos, P. Georgoudis, D. Lenis, N. Minkov, and C. Quesne, Phys. Lett. B **683**, 264 (2010).
[59] P. E. Georgoudis, Phys. Lett. B **731**, 122 (2014).
[60] D. Bonatsos, N. Minkov, and D. Petrellis, J. Phys. G **42**, 095104 (2015).
[61] E. T. Whittaker, Bull. Am. Math. Soc. **10**, 125 (1904).

[62] M. E. Rose, *Elementary Theory of Angular Momentum* (Wiley, New York, 1957).
[63] D. J. Rowe, J. Phys. A: Math. Gen. **38**, 10181 (2005).
[64] D. J. Rowe and P. S. Turner, Nucl. Phys. A **753**, 94 (2005).
[65] R. F. Casten, J. Phys. G: Nucl. Part. Phys. **42**, 034029 (2015).
[66] N. V. Zamfir and R. F. Casten, Phys. Lett. B **260**, 265 (1991).
[67] K. Kitao, Nucl. Data Sheets **75**, 99 (1995).
[68] K. Kitao, Y. Tendow, and A. Hashizume, Nucl. Data Sheets **96**, 241 (2002).
[69] T. Tamura, Nucl. Data Sheets **108**, 455 (2007).
[70] J. Katakura and Z. D. Wu, Nucl. Data Sheets **109**, 1655 (2008).
[71] J. Katakura and K. Kitao, Nucl. Data Sheets **97**, 765 (2002).
[72] Z. Elekes and J. Timar, Nucl. Data Sheets **129**, 191 (2015).
[73] NUDAT database, https://www.nndc.bnl.gov/nudat2/.